

Non-Boussinesq stability analysis of natural-convection gaseous flow on inclined hot plates

Prabakaran Rajamanickam^{a,*}, Wilfried Coenen^a, Antonio L. Sánchez^a

^a*Department of Mechanical and Aerospace Engineering, University of California San Diego, La Jolla, CA 92093-0411, USA*

Abstract

The buoyancy-driven boundary-layer flow that develops over a semi-infinite inclined hot plate is known to become unstable at a finite distance from the leading edge, characterized by a critical value of the Grashof number Gr based on the local boundary-layer thickness. The nature of the resulting instability depends on the inclination angle ϕ , measured from the vertical direction. For values of ϕ below a critical value ϕ_c the instability is characterized by the appearance of spanwise traveling waves, whereas for $\phi > \phi_c$ the bifurcated flow displays Görtler-like streamwise vortices. The Boussinesq approximation, employed in previous linear stability analyses, ceases to be valid for gaseous flow when the wall-to-ambient temperature ratio Θ_w is not close to unity. The corresponding non-Boussinesq analysis is presented here, accounting also for the variation with temperature of the different transport properties. A temporal stability analysis including nonparallel effects of the base flow is used to determine curves of neutral stability, which are then employed to delineate the dependences of the critical Grashof number and of its associated wave length on the inclination angle ϕ and on the temperature ratio Θ_w for the two instability modes, giving quantitative information of interest for configurations with $\Theta_w - 1 \sim 1$. The analysis provides in particular the predicted dependence of the crossover inclination angle ϕ_c on Θ_w , indicating that for gaseous flow with $\Theta_w - 1 \sim 1$ spanwise

*Corresponding author

Email address: prajaman@ucsd.edu (Prabakaran Rajamanickam)

traveling waves are predominant over a range of inclination angles $0 \leq \phi \leq \phi_c$ that is significantly wider than that predicted in the Boussinesq approximation.

Keywords: natural convection; inclined hot plate; non-Boussinesq effects; vortex instability; wave instability

1. Introduction

A semi-infinite inclined hot plate placed in a quiescent air atmosphere is known to induce near its surface a free-convection flow as a result of the action of buoyancy forces on the heated gas. The structure of the resulting boundary layer away from the plate edge exhibits at leading order a self-similar structure, as first noted in the experimental study of Schmidt and Beckmann [1]. This boundary layer is known to become unstable to small disturbances at a certain distance measured from the leading edge of the plate [2]. The character of the observed instability depends on the inclination angle ϕ , measured from the vertical direction. Thus, for values of ϕ above a critical value ϕ_c , including in particular horizontal and nearly horizontal plates, the instability develops in the form of stationary counter-rotating vortex rolls that are oriented in the streamwise direction. These are similar to those characterizing the Görtler instability of boundary-layer flow along a concave wall, driven by centrifugal forces, with the wall-normal component of the buoyancy force being the driving mechanism for free-convection flow. As the inclination angle ϕ is decreased, this wall-normal buoyancy component loses importance and, below a certain crossover angle ϕ_c , the character of the observed instabilities changes to Tollmien-Schlichting-like traveling waves driven by shear. Following existing terminology [3, 4], in the following the stability mode involving streamwise stationary vortices will be termed *vortex instability*, whereas that involving traveling waves will be termed *wave instability*.

Sparrow & Husar [2] were the first to identify both modes experimentally, and to show that their prevalence depends on the inclination of the heated surface. The crossover angle was determined by Lloyd & Sparrow [5] to lie

between $14^\circ < \phi_c < 17^\circ$. Other experiments carried out later agree generally with these findings [6–11].

Apart from the inclination angle ϕ , the buoyancy-induced flow over a semi-infinite flat plate at constant temperature depends on the Prandtl number Pr of the fluid and on the ratio $\Theta_w = T_w^*/T_\infty^*$ of the wall temperature to the ambient temperature. All previous theoretical efforts aimed at quantifying the critical conditions at the onset of the vortex and wave instabilities were performed in the Boussinesq approximation [3, 4, 12–20], which is only justified in gaseous flow when the wall-to-ambient relative temperature difference $(\Theta_w - 1)$ is small. Most of these studies employ linear local stability theory—a normal mode analysis—to determine, for fixed values of Pr and ϕ , the critical boundary-layer thickness δ_o^* , measured in dimensionless form through a local Grashof number, above which small perturbations, either of vortex type with associated spanwise wave number l^* , or of wave type with streamwise wave number k^* , are amplified. In this manner, a unique neutral curve in the Grashof – wave number plane can be delineated for each mode. The mode with the lowest corresponding critical Grashof number for all wave numbers would be the one that prevails in an experiment, and the value of that Grashof number would give the local boundary-layer thickness—and therefore the distance x^* to the plate edge—at which the instability first develops.

Conventionally, in a local stability analysis the base flow is assumed to be strictly parallel. That assumption must be reconsidered in the analysis of slowly varying slender flows, such as the present boundary layer, for which the order of magnitude of some of the terms in the stability equations, involving the transverse velocity component and the streamwise variation of the flow, is comparable to that of the viscous terms, and must be correspondingly taken into account. This so-called locally nonparallel approach was already adopted by Haaland & Sparrow in their temporal stability analyses of the vortex [3] and wave [4] instability modes. The resulting critical Grashof numbers were seen to differ by several orders of magnitude from those obtained with a strictly parallel analysis, thereby underlining the importance of the nonparallel terms. The problem was

re-examined by a series of authors, adopting small variations of this approach, either in a temporal [12, 13, 15–19] or a spatial [14] linear–stability framework. The analysis can be extended to describe finite-amplitude vortex rolls and secondary bifurcations by retaining selected nonlinear terms in the description, as done by Chen *et al.* [19]. Recently, instabilities in transient cooling of inclined surfaces and cavities have been studied numerically [21, 22].

The accuracy of the computations mentioned above deteriorates in the presence of order–unity deviations of the wall temperature from the ambient temperature, when the use of the Boussinesq approximation is no longer justified. Although non-Boussinesq effects have been taken into account in analyses of the boundary-layer structure for flow over a heated plate [23–25], these effects have never been considered in connection with the associated stability problem. The objective of the present work is to revisit the classical work of Haaland & Sparrow [3, 4], including the influence of the wall-to-ambient temperature ratio Θ_w for cases with $\Theta_w - 1 \sim 1$. In particular, a linear temporal modal stability analysis will be performed to investigate both the vortex and the wave modes, with account taken of nonparallel effects associated with the slow downstream evolution of the base flow. The effect of Θ_w on the neutral stability curves will be assessed, along with the dependence of the crossover angle defining the transition between the two types of instability.

The paper is structured as follows. The governing equations and boundary conditions for the base flow and for the linear stability analysis are given in §2. The vortex mode is studied in §3, followed in §4 by the analysis of the wave instability. The predictions of the critical conditions for the two modes are compared in §5 to delineate the boundary that defines the regions of prevalence of each mode on the parametric plane $\phi - \Theta_w$. Finally, concluding remarks are offered in §6.

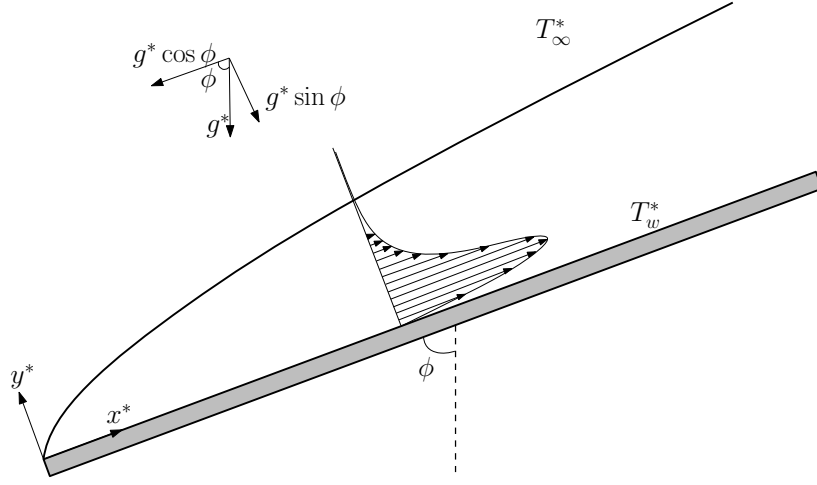


Figure 1: Schematic diagram of the boundary-layer flow over a heated inclined surface.

2. Problem formulation

The problem considered here, shown schematically in figure 1, involves the flow induced by buoyancy near the surface of a semi-infinite inclined plate whose temperature is held at a constant value, T_w^* , higher than the ambient temperature T_∞^* found in the surrounding quiescent air atmosphere. The associated velocities are negligibly small compared to the sound speed, so that the conservation equations can be written in the low-Mach number approximation

$$\frac{\partial \rho^*}{\partial t^*} + \nabla^* \cdot (\rho^* \mathbf{v}^*) = 0, \quad (1)$$

$$\rho^* \frac{\partial \mathbf{v}^*}{\partial t^*} + \rho^* \mathbf{v}^* \cdot \nabla^* \mathbf{v}^* = -\nabla^* p^* + (\rho^* - \rho_\infty^*) \mathbf{g}^* + \nabla^* \cdot [\mu^* (\nabla^* \mathbf{v}^* + \nabla^* \mathbf{v}^{*T})], \quad (2)$$

$$\rho^* \frac{\partial T^*}{\partial t^*} + \rho^* \mathbf{v}^* \cdot \nabla^* T^* = \frac{1}{Pr} \nabla^* \cdot (\mu^* \nabla^* T^*), \quad (3)$$

where ρ^* , \mathbf{v}^* , and T^* represent the density, velocity, and temperature of the gas; dimensional quantities are indicated everywhere in the text with an asterisk (*). In the momentum equation (2), p^* represents the sum of the pressure difference from the ambient hydrostatic distribution and the isotropic component of the stress tensor. Cartesian coordinates are used in the description,

including the streamwise distance measured along the plate from the leading edge x^* , the transverse distance from the surface of the plate y^* , and the spanwise coordinate z^* , with corresponding velocity components $\mathbf{v}^* = (u^*, v^*, w^*)$. The inclination angle ϕ is measured from the vertical, so that the gravity vector is $\mathbf{g}^* = -g^* \cos \phi \mathbf{e}_x - g^* \sin \phi \mathbf{e}_y$.

The above equations must be supplemented with the equation of state

$$\frac{\rho^*}{\rho_\infty^*} = \frac{T_\infty^*}{T^*} \quad (4)$$

and with the presumed power law

$$\frac{\mu^*}{\mu_\infty^*} = \frac{\kappa^*}{\kappa_\infty^*} = \left(\frac{T^*}{T_\infty^*} \right)^\sigma \quad (5)$$

for the temperature dependence of the viscosity and thermal conductivity, with the subscript ∞ denoting properties in the unperturbed ambient air. The constant values $Pr = 0.7$ and $\sigma = 2/3$, corresponding to air, will be used below for the Prandtl number $Pr = c_p^* \mu_\infty^* / \kappa_\infty^*$ in (3) and for the exponent σ in (5). Equations (1)–(3) must be integrated with the boundary conditions

$$\begin{cases} u^* = v^* = w^* = T^* - T_w^* = 0 & \text{at } y^* = 0 \text{ for } x^* > 0 \\ u^* = v^* = w^* = T^* - T_\infty^* = p^* = 0 & \text{as } (x^{*2} + y^{*2}) \rightarrow \infty \text{ for } y^* \neq 0, x^* > 0. \end{cases} \quad (6)$$

For plates that are not nearly horizontal, such that $\pi/2 - \phi$ is not small, the flow is driven by the direct acceleration associated with the gravity component parallel to the plate $g^* \cos \phi$. Near the leading edge of the plate there exists a nonslender Navier–Stokes region of characteristic size $[\nu_\infty^{*2} / (g^* \cos \phi)]^{1/3}$ where the velocity components are of order $(\nu_\infty^* g^* \cos \phi)^{1/3}$, with $\nu_\infty^* = \mu_\infty^* / \rho_\infty^*$ denoting the ambient kinematic viscosity, such that the local Reynolds number there is of order unity. Outside this Navier–Stokes region the flow–field structure includes a boundary-layer region of characteristic thickness $[(\nu_\infty^{*2} x^*) / (g^* \cos \phi)]^{1/4}$ and characteristic streamwise velocity $(g^* \cos \phi x^*)^{1/2}$, surrounded by an outer region of slow irrotational motion driven by the boundary-layer entrainment.

The stability of the boundary layer at a given location $x^* = x_o^*$ depends on

the value of the associated Grashof number

$$Gr = \frac{x_o^*}{\delta_o^*} = \frac{\delta_o^{*3} g^* \cos \phi}{\nu_\infty^{*2}} = \left(\frac{x_o^{*3} g^* \cos \phi}{\nu_\infty^{*2}} \right)^{1/4}, \quad (7)$$

which is the Reynolds number based on the local values of the thickness and streamwise velocity

$$\delta_o^* = \left(\frac{\nu_\infty^{*2} x_o^*}{g^* \cos \phi} \right)^{1/4} \quad \text{and} \quad u_o^* = (g^* \cos \phi x_o^*)^{1/2}. \quad (8)$$

The following analysis assumes implicitly that the critical value of Gr associated with the onset of the instability is moderately large, as corresponds to a location $x_o^*/\delta_o^* \gg 1$ far downstream from the Navier–Stokes region, where the flow near the plate surface is slender, enabling the stability analysis to be developed on the basis of the nearly parallel approximation, with the self-similar boundary-layer solution used to evaluate the base flow, as indicated below.

2.1. Base flow

The near-plate solution that develops outside the Navier–Stokes region can be described with small relative errors of order Gr^{-2} by using the boundary-layer form of the conservation equations. We shall neglect the pressure differences across the boundary layer, of order $\rho_\infty^* g^* \sin \phi \delta_o^*$, associated with the transverse component of the gravitational acceleration $g^* \sin \phi$, because they are small compared with the streamwise hydrostatic pressure differences $\rho_\infty^* g^* \cos \phi x_o^*$ at distances $x_o^* \gg \delta_o^* \tan \phi$, corresponding to local values of the Grashof number

$$Gr \gg \tan \phi, \quad (9)$$

a condition readily satisfied outside the Navier–Stokes region for the inclined plates with $\pi/2 - \phi \sim 1$ considered here. The resulting solution is self-similar when expressed in terms of the dimensionless coordinate

$$\eta = \frac{y^*}{[(\nu_\infty^{*2} x_o^*)/(g^* \cos \phi)]^{1/4}} \quad (10)$$

with use made of the nondimensional temperature and stream function

$$\Theta(\eta) = \frac{T^*}{T_\infty^*} \quad \text{and} \quad F(\eta) = \frac{\psi^*}{(x_o^{*3} \nu_\infty^{*2} g^* \cos \phi)^{1/4}}, \quad (11)$$

with associated self-similar velocity components

$$U = \frac{u^*}{(g^* \cos \phi x^*)^{1/2}} = \Theta F' \quad \text{and} \quad V = \frac{v^*}{(\nu_\infty^{*2} g^* \cos \phi / x^*)^{1/4}} = \frac{\Theta}{4} (\eta F' - 3F). \quad (12)$$

Here the prime is used to denote differentiation with respect to η . Introducing these variables reduces the problem to that of integrating

$$(\Theta^\sigma (\Theta F')')' + \frac{3}{4} F (\Theta F')' - \frac{1}{2} \Theta F'^2 + 1 - \frac{1}{\Theta} = 0, \quad (13)$$

$$(\Theta^\sigma \Theta')' + \frac{3}{4} Pr F \Theta' = 0, \quad (14)$$

with boundary conditions $F(0) = F'(0) = F'(\infty) = \Theta(0) - \Theta_w = \Theta(\infty) - 1 = 0$, where $\Theta_w = T_w^*/T_\infty^*$ is the wall-to-ambient temperature ratio.

The numerical integration was performed using a spectral collocation method with a fractional transformation defined by $y = a(1 + \xi)/(b - \xi)$ [26], where $a = y_c y_{\max}/(y_{\max} - 2y_c)$ and $b = 1 + 2a/y_{\max}$, that maps N Chebyshev collocation points $\xi \in [-1, 1]$ to the physical domain $y \in [0, y_{\max}]$ allocating $N/2$ collocation points to the near-wall region $0 < y < y_c$. Values $y_{\max} = 200$, $y_c = 15$ and $N = 128$ are found to be adequate, slightly higher than the values used in [20] for spatial analysis. Resulting temperature and velocity profiles are shown in figure 2 for different values of Θ_w , giving results similar to those presented elsewhere [25].

2.2. Linear stability analysis

Using standard practice, the linear stability of the flow at $x^* = x_o^*$ is investigated by introducing into (1)–(5) the perturbed nondimensional variables

$$\begin{aligned} \frac{\mathbf{v}^*}{u_o^*} &= \bar{\mathbf{v}}(x/Gr, y) + \mathbf{v}(x, y, z, t) = (\bar{u}, \bar{v}, 0) + (u, v, w) \\ \frac{T^*}{T_\infty^*} &= \bar{T}(x/Gr, y) + \theta(x, y, z, t) \\ \frac{\rho^*}{\rho_\infty^*} &= \bar{\rho}(x/Gr, y) + \rho(x, y, z, t) \\ \frac{\mu^*}{\mu_\infty^*} &= \bar{\mu}(x/Gr, y) + \mu(x, y, z, t) \\ \frac{p^*}{\rho_\infty^* u_o^{*2}} &= p(x, y, z, t) \end{aligned} \quad (15)$$

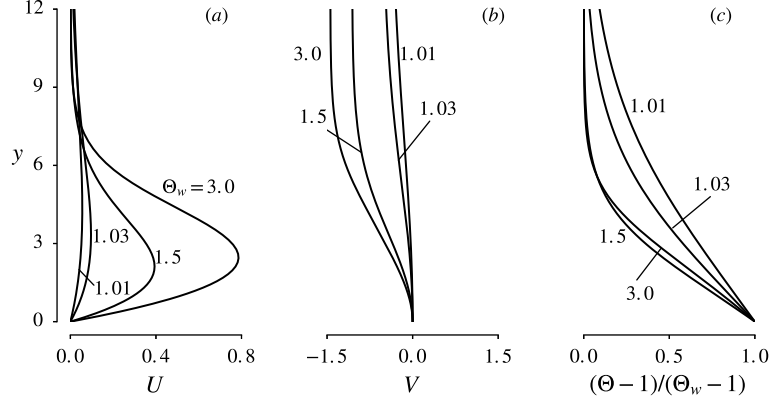


Figure 2: The self-similar base-flow solution obtained by integration of (13)–(14) with $Pr = 0.7$ and $\sigma = 2/3$ for different values of Θ_w .

where

$$x = \frac{x^* - x_o^*}{\delta_o^*}, \quad y = \frac{y^*}{\delta_o^*}, \quad z = \frac{z^*}{\delta_o^*}, \quad \text{and} \quad t = \frac{t^*}{\delta_o^*/u_o^*}, \quad (16)$$

leading to the linearized equations

$$\frac{\partial \rho}{\partial t} = -\bar{\rho} \nabla \cdot \mathbf{v} - \rho \nabla \cdot \bar{\mathbf{v}} - \mathbf{v} \cdot \nabla \bar{\rho} - \bar{\mathbf{v}} \cdot \nabla \rho, \quad (17)$$

$$\begin{aligned} \bar{\rho} \frac{\partial \mathbf{v}}{\partial t} = & -\bar{\rho} \bar{\mathbf{v}} \cdot \nabla \mathbf{v} - \bar{\rho} \mathbf{v} \cdot \nabla \bar{\mathbf{v}} - \rho \bar{\mathbf{v}} \cdot \nabla \bar{\mathbf{v}} - \nabla p - \frac{1}{Gr} \rho (\mathbf{e}_x + \tan \phi \mathbf{e}_y) \\ & + \frac{1}{Gr} \nabla \cdot [\bar{\mu} (\nabla \mathbf{v} + \nabla \mathbf{v}^T) + \mu (\nabla \bar{\mathbf{v}} + \nabla \bar{\mathbf{v}}^T)], \end{aligned} \quad (18)$$

$$\begin{aligned} \bar{\rho} \frac{\partial \theta}{\partial t} = & -\bar{\rho} \bar{\mathbf{v}} \cdot \nabla \theta - \bar{\rho} \mathbf{v} \cdot \nabla \bar{T} - \rho \bar{\mathbf{v}} \cdot \nabla \bar{T} \\ & + \frac{1}{Gr Pr} \nabla \cdot [\bar{\mu} \nabla \theta + \mu \nabla \bar{T}], \end{aligned} \quad (19)$$

and

$$\rho = -\bar{T}^{-2} \theta \quad \text{and} \quad \mu = \sigma \bar{T}^{\sigma-1} \theta. \quad (20)$$

The base profiles $\bar{\mathbf{v}}$, \bar{T} , $\bar{\rho}$, and $\bar{\mu}$ can be evaluated from the self-similar velocity

and temperature profiles $U(\eta)$, $V(\eta)$, and $\Theta(\eta)$ according to

$$\begin{aligned}\bar{u} &= (1 + x/Gr)^{1/2} U(y/[1 + x/Gr]^{1/4}), \\ \bar{v} &= Gr^{-1}(1 + x/Gr)^{-1/4} V(y/[1 + x/Gr]^{1/4}), \\ \bar{T} &= \frac{1}{\bar{\rho}} = \bar{\mu}^{1/\sigma} = \Theta(y/[1 + x/Gr]^{1/4}),\end{aligned}\tag{21}$$

written in terms of the local coordinates $x = (x^* - x_o^*)/\delta_o^*$ and $y = y^*/\delta_o^*$ by using $\eta = y/(1 + x/Gr)^{1/4}$ and $Gr = x_o^*/\delta_o^*$. As can be seen, the base flow displays a slow streamwise variation through the rescaled coordinate x/Gr . The expressions given above can be used to evaluate the factors that appear in the linearized equations (17)–(19). In the first approximation for $Gr \gg 1$ one obtains the order-unity factors

$$\begin{aligned}\bar{u} &= U(y), \quad \frac{\partial \bar{u}}{\partial y} = U'(y), \quad \frac{\partial^2 \bar{u}}{\partial y^2} = U''(y), \\ \bar{T} &= \frac{1}{\bar{\rho}} = \bar{\mu}^{1/\sigma} = \Theta(y), \quad \frac{\partial \bar{T}}{\partial y} = \Theta'(y), \quad \frac{\partial^2 \bar{T}}{\partial y^2} = \Theta''(y),\end{aligned}\tag{22}$$

which pertain to the strictly parallel flow, along with the factors of order Gr^{-1}

$$\begin{aligned}\bar{v} &= Gr^{-1}V(y), \quad \frac{\partial \bar{v}}{\partial y} = Gr^{-1}V'(y), \quad \frac{\partial \bar{u}}{\partial x} = Gr^{-1} \left[\frac{1}{2}U(y) - \frac{y}{4}U'(y) \right], \\ \frac{\partial \bar{T}}{\partial x} &= -Gr^{-1} \frac{y}{4} \Theta'(y), \quad \text{and} \quad \frac{\partial \bar{\rho}}{\partial x} = Gr^{-1} \frac{y}{4} \frac{\Theta'(y)}{\Theta^2(y)},\end{aligned}\tag{23}$$

arising from nonparallel effects.

The nearly parallel stability analysis performed here assumes implicitly a moderately small value of Gr^{-1} , a condition needed to ensure the slenderness of the flow. The small parameter Gr^{-1} appears in (17)–(19) directly as a factor in the molecular transport terms in (18) and (19) and also through the factors (23) associated with the slow streamwise variation of the base flow. If only terms of order unity are retained in (17)–(19), then the resulting equations describe the inviscid instability of strictly parallel flow. By retaining also terms of order Gr^{-1} one accounts simultaneously for viscous and nonparallel effects, that being the approach pursued herein. Thus, following Haaland & Sparrow [3, 4], the equations (17)–(19) were systematically simplified by retaining terms up to $O(Gr^{-1})$, while neglecting terms of order Gr^{-2} and higher. The

resulting simplified equations are written in Appendix A for the normal-mode perturbations

$$[u, v, w, p, \theta, \rho, \mu](x, y, z, t) = e^{i(kx+lz-\omega t)}[\hat{u}, \hat{v}, \hat{w}, \hat{p}, \hat{\theta}, \hat{\rho}, \hat{\mu}](y), \quad (24)$$

where k and l are the dimensionless streamwise and spanwise wave numbers, and $\omega = \omega_r + i\omega_i$ contains both the frequency ω_r and the growth rate ω_i of the perturbations. The vortex instability is associated with modes with $k = 0$ and $\omega_r = 0$, whereas the wave instability corresponds to $l = 0$ and $\omega_r > 0$. The two types of instabilities will be studied separately in the following two sections.

3. Vortex instability

3.1. The simplified eigenvalue problem

We start by considering instabilities characterized by the appearance of Görtler-like vortex rolls aligned with the streamwise direction, known to dominate the boundary-layer dynamics for values of ϕ above a critical value ϕ_c . These can be investigated by setting $k = 0$ in the normal-mode ansatz (24). Chen *et al.* [19] showed that the principle of exchange of instabilities holds for this type of instabilities, in the sense that in the full eigenvalue spectrum the eigenvalue with the largest growth rate ω_i has zero frequency $\omega_r = 0$. Hence, the critical conditions for vortex instability can be computed by setting both k and ω equal to zero in (A.1)–(A.5). Eliminating then \hat{p} and \hat{w} by combining equations (A.1), (A.3) and (A.4), and introducing the transformation

$$\tilde{u} = \hat{u} \tan \phi, \quad \tilde{v} = \hat{v}, \quad \tilde{\theta} = \hat{\theta} \tan \phi, \quad \tilde{Gr} = Gr \tan \phi \quad (25)$$

to remove the explicit dependence on the inclination angle ϕ [3], leads to the three equations

$$[\mathbf{D}(\Theta^\sigma \mathbf{D}) - (V/\Theta)\mathbf{D} - (2U - yU')/(4\Theta)] \tilde{u} + \{[1 + VU' + U(2U - yU')/4]/\Theta^2 + \sigma\Theta^{\sigma-1}(U'\mathbf{D} + U'')\} \tilde{\theta} = \tilde{G}r \frac{U'}{\Theta} \tilde{v}, \quad (26)$$

$$\mathbf{D} \left[\frac{1}{l^2} \left(\mathbf{D}\Theta^\sigma - \frac{V}{\Theta} \right) \mathbf{D} \left(\mathbf{D} - \frac{\Theta'}{\Theta} \right) + \mathbf{D}\Theta^\sigma - 2\Theta^\sigma \left(2\mathbf{D} - \frac{\Theta'}{\Theta} \right) \right] \tilde{v} + \left[\Theta^\sigma \mathbf{D} \left(\mathbf{D} - \frac{\Theta'}{\Theta} \right) + \frac{1}{\Theta} (\mathbf{D}V) + \Theta^\sigma l^2 \right] \tilde{v} - \Theta^{-2} \tilde{\theta} = 0, \quad (27)$$

$$\left[\mathbf{D}(\Theta^\sigma \mathbf{D}) + \sigma(\mathbf{D}\Theta^{\sigma-1}\Theta') - Pr \frac{V}{\Theta} \mathbf{D} - \Theta^\sigma l^2 - Pr \left(\frac{y}{4} U - V \right) \frac{\Theta'}{\Theta^2} \right] \tilde{\theta} + Pr \frac{y\Theta'}{4\Theta} \tilde{u} = \tilde{G}r Pr \frac{\Theta'}{\Theta} \tilde{v}, \quad (28)$$

with boundary conditions

$$\tilde{u} = \tilde{v} = \mathbf{D}\tilde{v} = \tilde{\theta} = 0 \quad \text{at } y = 0 \text{ and as } y \rightarrow \infty. \quad (29)$$

In the operators acting on the eigenfunctions the symbol \mathbf{D} denotes differentiation with respect to y . A function of y placed immediately after \mathbf{D} indicates that multiplication by that function should be performed prior to differentiation, so that, for instance, $(\mathbf{D}\Theta^\sigma)\tilde{v} = \mathbf{d}(\Theta^\sigma\tilde{v})/\mathbf{d}y$, while $(\Theta^\sigma\mathbf{D})\tilde{v} = \Theta^\sigma \mathbf{d}\tilde{v}/\mathbf{d}y$ instead. The eigenfunction \tilde{u} is coupled to \tilde{v} and $\tilde{\theta}$ through the last term on the left-hand side in (28), associated with the slow streamwise variation of the base temperature \bar{T} . Also of interest is that for strictly parallel flow (i.e., when the factors listed in (23) are set equal to zero), the problem becomes independent of the base velocity field, and the resulting equations reduce to those corresponding to Rayleigh-Bénard convection.

3.2. Numerical results

For a given wall-to-ambient temperature ratio Θ_w , which defines the base flow, and a given spanwise wave number l , the above eigenvalue problem (26)–(29) was solved numerically to determine the critical value $\tilde{G}r_0$ of $\tilde{G}r$ identifying the conditions of neutral stability. The variation of $\tilde{G}r_0 = \tan\phi Gr_0$ with l is shown in figure 3(a) for different Θ_w . As can be seen, each neutral curve $\tilde{G}r_0(l)$

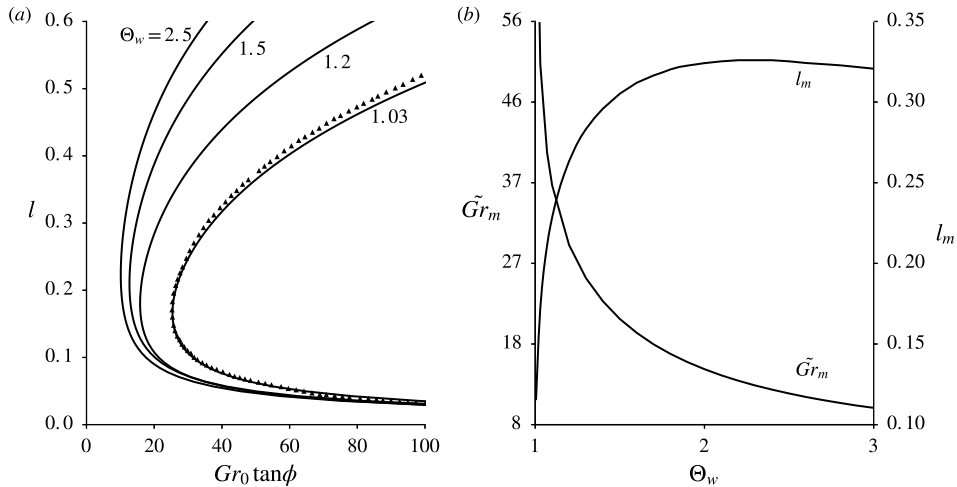


Figure 3: Results of the non-Boussinesq analysis of the vortex instability, including curves of neutral stability (a) along with the variation with Θ_w of $\tilde{G}r_m$ and of the associated spanwise wave number l_m (b); the triangles in (a) corresponds to evaluations of (30) with the values of Gr_B reported in [3] (corrected to account for the factor 4 used in their definition of the boundary-layer thickness δ_o^*).

reaches a minimum value $\tilde{G}r_0 = \tilde{G}r_m$ at $l = l_m$. This minimum determines the wave length $2\pi/l_m$ of the most unstable mode along with the downstream location $x_m^* = (\tilde{G}r_m / \tan \phi)^{4/3} [\nu_\infty^{*2} / (g^* \cos \phi)]$ at which the vortices begin to develop. To complete the description, the variation of $\tilde{G}r_m$ and l_m for the most unstable mode is plotted as a function of Θ_w in figure 3(b). It is evident from the plots that increasing the wall-to-ambient temperature ratio Θ_w as well as increasing ϕ towards a more horizontal position tends to destabilize the flow. Also noteworthy is the rapid variation of $\tilde{G}r_m$ and l_m with Θ_w for $\Theta_w - 1 \ll 1$.

3.3. Departures from the Boussinesq approximation

The results can be compared to the Boussinesq analysis of Haaland & Sparrow [3] by taking a wall-to-ambient temperature ratio Θ_w close to unity. The Boussinesq Grashof number employed in [3], $Gr_B = [\beta^*(T_w^* - T_\infty^*)x^*{}^3 g^* \cos \phi / \nu_\infty^{*2}]^{1/4}$, is related to that defined in (7) by $Gr_B = Gr[\beta^*(T_w^* - T_\infty^*)]^{1/4}$. The result depends on the temperature used to evaluate the coefficient of thermal expansion

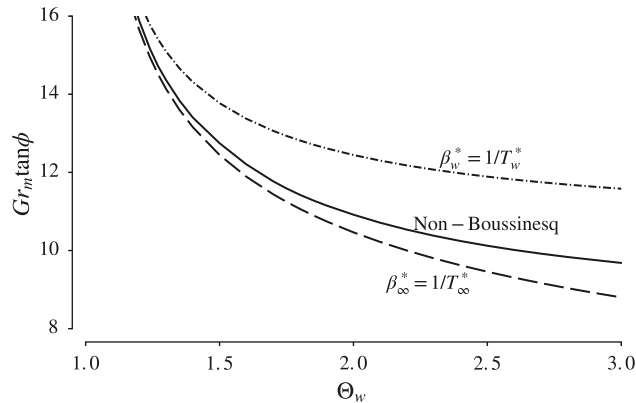


Figure 4: The variation of $Gr_m \tan \phi$ with Θ_w obtained from integrations of the non-Boussinesq eigenvalue problem (26)–(29) (solid curve) and from the Boussinesq predictions (30) and (30) evaluated with $Gr_B = 10.5$, obtained by scaling the value given in [3], as indicated in the text.

β^* , given for an ideal gas by $\beta^* = 1/T^*$. Thus, using the ambient temperature to evaluate $\beta_\infty^* = 1/T_\infty^*$ yields

$$Gr_w = Gr_B(\Theta_w - 1)^{-1/4} \quad (30)$$

whereas the expression

$$Gr_\infty = Gr_B(1 - \Theta_w^{-1})^{-1/4} \quad (31)$$

is obtained by using the wall temperature to evaluate $\beta_w^* = 1/T_w^*$. Clearly, the temperature selected to define β^* becomes irrelevant for $\Theta_w - 1 \ll 1$, when the relative differences between both expressions are of order $(\Theta_w - 1)/4$. Equation (30) is selected in the comparison of figure 3(a) to evaluate the neutral curve for $\Theta_w = 1.03$ using the values of Gr_B reported in Haaland & Sparrow [3], giving the results represented by the triangles.

As can be seen in figure 3(a), the differences between the predictions obtained with the Boussinesq approximation and those accounting for non-Boussinesq effects are very small for $\Theta_w = 1.03$, with departures in resulting values of \tilde{Gr}_m and l_m of the order of 1%. The departures are expected to become larger for increasing values of $\Theta_w - 1$, with the two expressions (30) and (31) leading to

increasingly different values of Gr . This is tested in figure 4 by comparing the curve $\tilde{Gr}_m - \Theta_w$ obtained from the numerical integrations of (26)–(29), given previously in figure 3(b), with the predictions derived by extending the Boussinesq approximation with use made of (30) and (31) evaluated with $Gr_B = 10.5$, the latter obtained by dividing the value 29.6 reported in [3] by $2\sqrt{2}$, as is needed to account for the factor 4 used in their definition of the boundary-layer thickness δ^* . As can be seen, our results lie between the two Boussinesq predictions, with the thermal expansion based on the ambient temperature $\beta_\infty^* = 1/T_\infty^*$ giving better agreement. For the vortex mode, it is apparent from the curves in the figure that straightforward extension of the stability results computed in the Boussinesq approximation by use of (31) provides sufficiently accurate predictions for the critical Grashof number even for configurations with $\Theta_w - 1 \sim 1$. As seen below, the wave mode analyzed next is different in this connection, in that the sharp decrease in \tilde{Gr}_m found for increasing Θ_w cannot be predicted by simply extending the results of the Boussinesq approximation, regardless of the temperature used in evaluating the thermal-expansion coefficient.

4. Wave instability

The wave instability on hot inclined plates has received significantly less attention [4, 14, 16, 20] than the related vortex instability problem, possibly because for Boussinesq flow its occurrence is restricted to a moderately small angle range $0^\circ < \phi \lesssim 20^\circ$ about the vertical position. In this connection, it is worth anticipating that the present analysis will show that this range widens significantly for non-Boussinesq gaseous flow with $\Theta_w - 1 \sim 1$.

4.1. The simplified eigenvalue problem

In accordance with Squire’s theorem, only two-dimensional disturbances need to be considered below, so that $l = 0$ in (24). Although a spatial stability analysis is needed to accurately determine the downstream growth rate of the disturbance [14, 20], the present work focuses on the determination of the

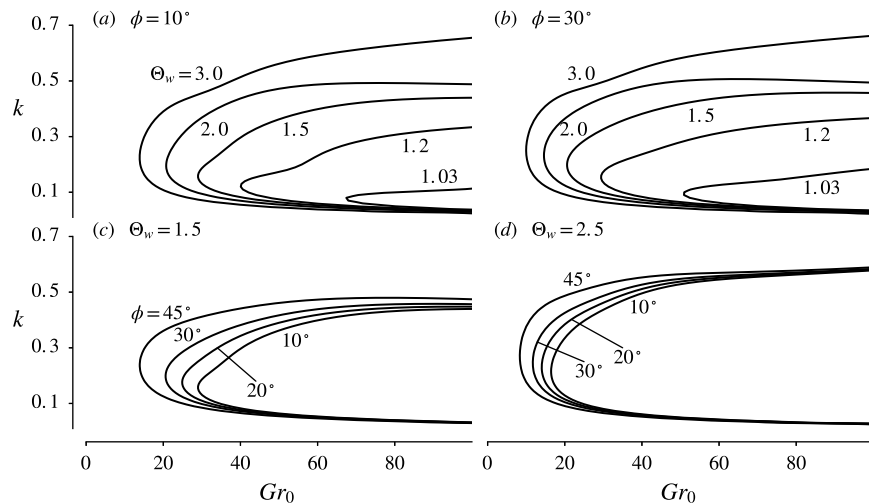


Figure 5: Curves of neutral stability for the wave mode with different wall-to-ambient temperature ratios Θ_w and different inclination angles ϕ .

curves of neutral stability, associated with real values of both the wave number k and the frequency ω , which can be obtained with a simpler temporal stability analysis.

With $l = 0$ the problem simplifies, in that the solution for \hat{u} , \hat{v} , \hat{p} , and $\hat{\theta}$ becomes independent of \hat{w} , so that the eigenvalue problem reduces to the solution of (A.1)–(A.3) and (A.5) with the homogeneous boundary conditions

$$\hat{u} = \hat{v} = \hat{\theta} = 0 \text{ at } y = 0, \quad \text{and} \quad \hat{u}, \hat{v}, \hat{\theta}, \hat{p} \rightarrow 0 \text{ as } y \rightarrow \infty. \quad (32)$$

The eigenvalue nature of this problem becomes more apparent by casting the equations in the standard form $A\mathbf{f} = \omega B\mathbf{f}$, with A and B being linear differential operators acting on $\mathbf{f} = (\hat{u}, \hat{v}, \hat{p}, \hat{\theta})$. As a result of the non-Boussinesq character of the continuity equation, elimination of \hat{p} and \hat{u} by linear combinations leads to a quadratic eigenvalue problem for the eigenvalue ω , which is not further considered here because of the additional complications involved in its numerical solution.

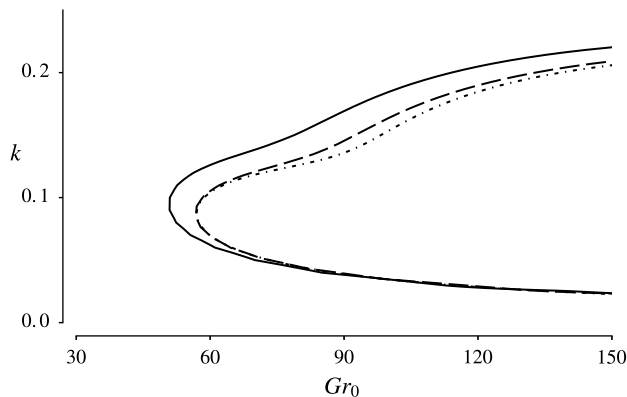


Figure 6: Curves of neutral stability for the wave-instability mode with $\Theta_w = 1.03$ and $\phi = 30^\circ$ obtained from (A.1), (A.5) and (33) (solid curve) and by repeating the computations with the underlined term removed in (33) (dashed curve); the dotted curve corresponds to evaluations of (30) with the values of Gr_B reported in [4].

4.2. Critical curves of neutral stability

Results obtained by integrating numerically the eigenvalue problem for the wave instability are shown in figure 5. Unlike the vortex instability, for which the dependence on the inclination angle can be scaled out of the equations by the transformation (25), thereby reducing the parametric dependence of the results, the eigenvalue problem for the wave instability depends on both ϕ and Θ_w . Curves of neutral stability are plotted in figures 5(a) and 5(b) for a fixed inclination angle ϕ and different values of the wall temperature ratio Θ_w , with corresponding curves for fixed Θ_w and different values of ϕ given in figures 5(c) and 5(d). Just as for the vortex instability, increasing the wall-to-ambient temperature ratio, as well as increasing the inclination angle (a more horizontal plate) has a destabilizing effect on the flow. The rapid change in the neutral curves shown in the upper plots of the figure as the wall temperature increases from $\Theta_w = 1.03$ to $\Theta_w = 1.2$ is indicative of the importance of non-Boussinesq effects for wave instability.

4.3. Stability predictions based on vorticity–stream function formulation

Before continuing the discussion of results, it is worth commenting on the differences arising from the use of different starting conservation equations in the presence of a slowly varying base flow. Unlike many previous analyses, which were derived on the basis of a vorticity–stream function formulation, the present analysis employs as a starting point the conservation equations written in primitive variables. Although the logical expectation is that both approaches yield the same results, that being the case for strictly parallel base flow, small but noticeable discrepancies were found between both computational approaches when the nonparallel terms are retained for the base flow. This is so because when the pressure is eliminated from the equations written in primitive variables *after* the normal mode decomposition is introduced, i.e. from equations (A.1)–(A.5), to obtain a normal-mode vorticity form, the resulting set of equations is not identical to that obtained by writing the momentum equation in terms of the vorticity *before* introducing the normal mode decomposition. This discrepancy does not happen when analyzing the vortex mode, because the direction of the vorticity differs between the base flow and the perturbations, i.e. the base-flow vorticity is oriented along the spanwise direction while the perturbed vorticity is oriented along the streamwise direction.

These differences can be illustrated by comparing the results of our formulation for $\Theta_w \ll 1$ with those obtained earlier by Haaland & Sparrow [4] using the linearized vorticity–stream function Boussinesq formalism presented earlier in [27]. The comparison can be readily established by writing our equations (A.2) and (A.3) for $\Theta_w - 1 \ll 1$ followed by elimination of the pressure to yield

$$\begin{aligned} & [D^3 - VD^2 - Gr i(Uk - \omega)D - k^2D + V'']\hat{u} \\ & [-ikD^2 + ikVD - Gr k(Uk - \omega) - GrU'' + ik^3 + \underline{ikV'}]\hat{v} + [D - ik \tan \phi]\hat{\theta} = 0 \end{aligned} \quad (33)$$

after the continuity equation is used to simplify the result. Comparing the above equation with equation (15) in [27] reveals that both are identical, except for the underlined term in (33), which is absent in [27], that being a consequence of

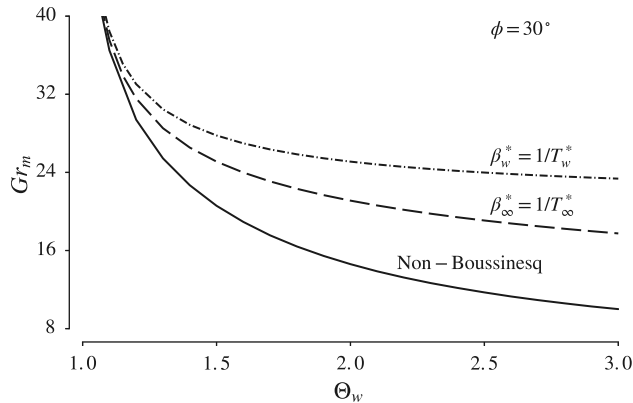


Figure 7: The variation of Gr_m with Θ_w for $\phi = 30^\circ$ obtained for the wave instability from integrations of the non-Boussinesq eigenvalue problem (solid curve) and from the Boussinesq predictions (30) and (31) evaluated with $Gr_B = 17.96$, the latter computed by extrapolating the numerical results as $\Theta_w \rightarrow 1$.

the different derivation procedure. As previously mentioned, the missing term, proportional to the transverse gradient of the transverse base velocity, would be absent for strictly parallel flow. Its quantitative importance is assessed in figure 6, where the neutral curve obtained using (A.1) and (A.5) together with (33) (solid curve) is compared with that obtained after selectively removing the term ikV' in (33) (dashed curve). The additional term is seen to destabilize the flow, resulting in critical Grashof numbers that are about 10% smaller than those obtained on the basis of the vorticity–stream function formulation. As expected, the dashed curve is seen to agree with that obtained by evaluating (30) with the values of Gr_B reported in Haaland & Sparrow [4] for $\phi = 30^\circ$, represented by a dotted line in figure 6.

4.4. Quantitative assessment of non-Boussinesq effects

To complete the description, the Boussinesq predictions (30) and (31) are compared in figure 7 with the results of the non-Boussinesq eigenvalue problem for $\phi = 30^\circ$. The value $Gr_B = 21.11$ used in the evaluations of (30) and (31) is extracted from our numerical results for $\Theta_w - 1 \ll 1$. Because of the discrepancies illustrated in figure 6, this value is somewhat smaller than the value

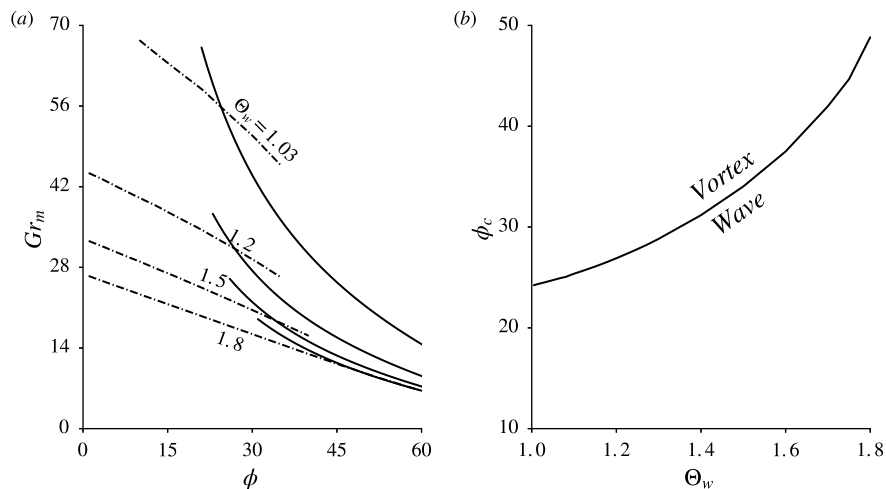


Figure 8: The left-hand-side plot represents the variation of the critical Grashof number with the inclination angle for the wave mode (dashed curves) and for the vortex mode (solid curves) for different values of the wall-to-ambient temperature ratio Θ_w , while the right-hand-side plot gives the variation with Θ_w of the crossover angle ϕ_c at which each pair of curves crosses.

reported in [4], which gives $Gr_B = 23.63$ once corrected to account for differences in their definition of δ^* . As can be seen in figure 7, the extrapolations of the Boussinesq results consistently overpredict the critical Grashof number. This is so because the Boussinesq approximation does not describe accurately the acceleration of the light gas for increasing Θ_w , which is apparent in the velocity profiles in figure 2, resulting in augmented shear stresses that trigger the wave-mode instability.

5. Variation of the crossover angle

It is apparent from the comparison of the curves in figures 4 and 7 that non-Boussinesq effects have a larger influence on the wave mode than they have on the vortex mode. For both modes, increasing the plate temperature promotes instability by decreasing the associated critical Grashof number, but the decrease of Gr_m is much more pronounced for the wave mode, thereby suggesting that the character of the instability that develops over a plate at a

given inclination angle may switch from a vortex mode to a wave mode as the plate temperature increases.

To investigate this aspect of the problem we compare in figure 8(a) the curves $Gr_m = \tilde{G}r_m / \tan \phi$ corresponding to the vortex mode, with $\tilde{G}r_m(\Theta_w)$ given in figure 3(b), with the values of Gr_m obtained from the turning points of the neutral curves computed for the wave mode for a fixed value of Θ_w , given for instance in figure 5(c) for the particular case $\Theta_w = 1.5$. The crossing point of each pair of curves determines the angle ϕ_c at which the character of the most unstable mode changes from a traveling wave (for $\phi < \phi_c$) to stationary streamwise vortices (for $\phi > \phi_c$). The resulting crossover angle increases for increasing Θ_w , as shown in figure 8(b), which delineates the parametric regions where each one of the modes prevails.

Our linear stability analysis predicts a crossover angle $\phi_c = 23.8^\circ$ for $\Theta_w - 1 \ll 1$, in agreement with the value $\phi_c = 22^\circ$ reported in previous linear stability analyses [15, 16] using instead the scalings of the horizontal boundary layer for the self-similar base flow. A somewhat smaller value was estimated in the work of Kahawita and Meloney [13] by evaluating approximately the critical Grashof number of the wave mode from the results of the vertical plate through simple multiplication by $\cos \phi$. It is worth noting that the values observed in experiments are typically somewhat smaller than the theoretical predictions (e.g., values in the range $14^\circ < \phi_c < 17^\circ$ are reported in the early work [5]). The deviations are attributable to the limitations of the linear analysis performed here, although more work is needed to clarify this issue.

As the value of Θ_w increases the crossing points of the curves in figure 8(a) moves to the right, corresponding a wider range $0 \leq \phi < \phi_c$ where the wave mode prevails. Unexpectedly, the two curves $Gr_m - \phi$ become tangent at $\Theta_w \simeq 1.8$ and exhibit no crossing point for larger values of $\Theta_w > 1.8$, for which our analysis predicts the wave mode to be dominant for all angles. Clearly, however, this prediction would need to be reconsidered for near-horizontal plates with values of ϕ approaching $\pi/2$, for which the condition (9), used in deriving the governing equations for the inclined plate, would no longer hold. A

revised stability analysis, accounting for transverse pressure differences across the boundary layer in deriving the governing equations for both the base flow and its perturbations, would be needed to assess the transition between both instability modes for very hot plates with $\Theta_w > 1.8$.

6. Concluding remarks

Although the existing experimental evidence and the previous theoretical predictions based on the Boussinesq approximation indicate that at higher wall temperatures the flow tends to become unstable at lower values of the Grashof number, corresponding to smaller downstream distances from the plate edge, quantitative results for relative wall-to-ambient temperature differences of order unity are not currently available. This paper provides the needed quantification on the basis of a non-Boussinesq temporal stability analysis accounting for the slow variation of the base flow. The results provide predictions of critical Grashof numbers for both modes of instability and their associated wave numbers. While non-Boussinesq effects are found to have only a moderate quantitative effect on the instability mode involving streamwise vortices, it is found that the augmented shear resulting from the flow acceleration in the presence of large density differences promotes wave instabilities significantly. As a result, the range of angles about the vertical position where the wave mode is dominant is predicted to increase substantially with increasing wall temperatures, a finding of our linear stability analysis that warrants future experimental investigation.

The characteristics of the analysis presented, both linear and local, limit the accuracy of some of the predictions. For instance, the nonlinear growth of the perturbations, not described herein, may explain the discrepancies between the predicted value of $\phi_c = 23.8^\circ$ for $\Theta_w - 1 \ll 1$ and previous experimental observations. Also, although the analysis accounts for the slow streamwise variation of the base flow in (15), the shape functions of the accompanying perturbations, as well as the wave numbers k and l are not allowed to depend on the rescaled

coordinate x/Gr , as would be needed to account for their downstream evolution. Incorporating the latter, while still taking advantage of the slenderness of the boundary-layer flow associated with moderately large values of the Grashof number—thus retaining only terms up to $\mathcal{O}(Gr^{-1})$ —would turn the *local* stability problem into a *nonlocal* parabolic stability problem that has to be integrated in the downstream direction. In this type of treatment a unique neutral curve cannot be defined since the streamwise development depends strongly on the initial conditions that are imposed at a certain location, as pointed out for the first time by Hall [28] for the related problem of Görtler instability over a curved wall. Subsequent studies [29] have found that, although different initial conditions result in different growth rates during the transient stage, at very large downstream distances the local growth rate is found to be independent of the initially imposed disturbance. Although an attempt to apply these concepts to the present problem was made by Tumin [20], more work is clearly needed to further clarify the instability characteristics of natural-convection flows.

A global stability analysis of the natural-convection flow under consideration, in which the instabilities are considered as two-dimensional temporal Fourier modes, is also worth pursuing in future work. Since this alternative approach does not invoke the slenderness condition of the basic flow, it might prove useful to study cases with very large wall-to-ambient temperature ratios, for which, as shown in the present work, the instability sets in at smaller Grashof numbers, and thus at shorter distances from the leading edge. The highly nonparallel Navier-Stokes region close the edge of the plate then may play an important role in these early transition events.

Acknowledgements

We would like to thank one of the reviewers for constructive comments and suggestions for relevant references.

Appendix A. Stability equations

Introducing the normal-mode decomposition (24) into (17)–(20) with $\hat{\rho} = -\Theta^{-2}\hat{\theta}$ and $\hat{\mu} = \sigma\Theta^{\sigma-1}\hat{\theta}$ and discarding terms of order Gr^{-2} yields

$$\begin{aligned} & [Gr\,ik\Theta^{-1} + (y/4)\Theta^{-2}\Theta']\hat{u} + Gr(D\Theta^{-1})\hat{v} + Gr\,il\Theta^{-1}\hat{w} \\ & - [DV + Gr\,i(Uk - \omega) + (2U - yU')/4]\Theta^{-2}\hat{\theta} = 0, \end{aligned} \quad (\text{A.1})$$

$$\begin{aligned} & [D(\Theta^\sigma D) - \Theta^{-1}VD - Gr\,i\Theta^{-1}(Uk - \omega) - \Theta^{-1}(2U - yU')/4 \\ & - \Theta^\sigma(2k^2 + l^2)]\hat{u} + [ik(D\Theta^\sigma) - Gr\Theta^{-1}U']\hat{v} - kl\Theta^\sigma\hat{w} - Gr\,ik\hat{p} \\ & + [\sigma(DU'\Theta^{\sigma+1}) + U(2U - yU')/4 + VU' + 1]\Theta^{-2}\hat{\theta} = 0, \end{aligned} \quad (\text{A.2})$$

$$\begin{aligned} & (ik\Theta^\sigma D)\hat{u} + [2D(\Theta^\sigma D) - \Theta^{-1}(DV) - Gr\,i\Theta^{-1}(Uk - \omega) - \Theta^\sigma(k^2 + l^2)]\hat{v} \\ & + (il\Theta^\sigma D)\hat{w} - Gr\,D\hat{p} + (\tan\phi\Theta^{-2} + \sigma\,ikU'\Theta^{\sigma-1})\hat{\theta} = 0, \end{aligned} \quad (\text{A.3})$$

$$\begin{aligned} & - \Theta^\sigma kl\hat{u} + il(D\Theta^\sigma)\hat{v} + [D(\Theta^\sigma D) - \Theta^{-1}VD \\ & - Gr\,i\Theta^{-1}(Uk - \omega) - \Theta^\sigma(k^2 + 2l^2)]\hat{w} - Gr\,il\hat{p} = 0, \end{aligned} \quad (\text{A.4})$$

$$\begin{aligned} & (Pr\Theta^{-1}\Theta'y/4)\hat{u} - GrPr\Theta^{-1}\Theta'\hat{v} + [D(\Theta^\sigma D + \sigma\Theta'\Theta^{\sigma-1}) - Pr\Theta^{-1}VD \\ & - GrPr\,i\Theta^{-1}(Uk - \omega) - \Theta^\sigma(k^2 + l^2) + Pr(V - Uy/4)\Theta^{-2}\Theta']\hat{\theta} = 0, \end{aligned} \quad (\text{A.5})$$

to be integrated with boundary conditions

$$\hat{u} = \hat{v} = \hat{w} = \hat{\theta} = 0 \text{ at } y = 0, \quad \text{and} \quad \hat{u} = \hat{v} = \hat{w} = \hat{\theta} = \hat{p} = 0 \text{ as } y \rightarrow \infty. \quad (\text{A.6})$$

As in the main text, the symbol D denotes differentiation with respect to y . In the convention adopted a function of y placed after D indicates that multiplication by that function should be performed prior to differentiation.

References

References

- [1] E. Schmidt, N. Beckmann, Das temperature and geschwindigkeitsfeld von einer warmeabgebenden senkrechten platte bei naturlicher konvektion, Tech. Mech. Thermodynamic 1 (1930) 341–349, 391–406.

- [2] E. Sparrow, R. Husar, Longitudinal vortices in natural convection flow on inclined plates, *J. Fluid Mech.* 37 (02) (1969) 251–255.
- [3] S. Haaland, E. Sparrow, Vortex instability of natural convection flow on inclined surfaces, *Int. J. Heat Mass Transfer.* 16 (12) (1973) 2355–2367.
- [4] S. Haaland, E. Sparrow, Wave instability of natural convection on inclined surfaces accounting for nonparallelism of the basic flow, *J. Heat Transfer.* 95 (3) (1973) 405–407.
- [5] J. Lloyd, E. Sparrow, On the instability of natural convection flow on inclined plates, *J. Fluid Mech.* 42 (03) (1970) 465–470.
- [6] H. Shaukatullah, B. Gebhart, An experimental investigation of natural convection flow on an inclined surface, *Int. J. Heat Mass Transfer.* 21 (12) (1978) 1481–1490.
- [7] K. Cheng, Y. Kim, Flow visualization studies on vortex instability of natural convection flow over horizontal and slightly inclined constant-temperature plates, *J. Heat Transfer.* 110 (3) (1988) 608–615.
- [8] E. Zuercher, J. Jacobs, C. Chen, Experimental study of the stability of boundary-layer flow along a heated, inclined plate, *J. Fluid Mech.* 367 (1998) 1–25.
- [9] P. Jeschke, H. Beer, Longitudinal vortices in a laminar natural convection boundary layer flow on an inclined flat plate and their influence on heat transfer, *J. Fluid Mech.* 432 (2001) 313–339.
- [10] M. Trautman, A. Glezer, The manipulation of the streamwise vortex instability in a natural convection boundary layer along a heated inclined flat plate, *J. Fluid Mech.* 470 (2002) 31–61.
- [11] F. Kimura, K. Kitamura, M. Yamaguchi, T. Asami, Fluid flow and heat transfer of natural convection adjacent to upward-facing, inclined, heated plates, *Heat Transfer - Asian Research.* 32 (3) (2003) 278–291.

- [12] G. Hwang, K. Cheng, Thermal instability of laminar natural convection flow on inclined isothermal plates, *The Canadian J. Chemical Eng.* 51 (6) (1973) 659–666.
- [13] R. Kahawita, R. Meroney, The vortex mode of instability in natural convection flow along inclined plates, *Int. J. Heat Mass Transfer.* 17 (5) (1974) 541–548.
- [14] P. Iyer, R. Kelly, The stability of the laminar free convection flow induced by a heated inclined plate, *Int. J. Heat Mass Transfer.* 17 (4) (1974) 517–525.
- [15] T. Chen, K. Tzuoo, Vortex instability of free convection flow over horizontal and inclined surfaces, *J. Heat Transfer.* 104 (4) (1982) 637–643.
- [16] K. L. Tzuoo, T. S. Chen, B. F. Armaly, Wave instability of natural convection flow on inclined surfaces, *J. Heat Transfer.* 107 (1) (1985) 107–111.
- [17] M. Lin, Numerical study of formation of longitudinal vortices in natural convection flow over horizontal and inclined surfaces, *Int. J. Heat Mass Transfer.* 44 (9) (2001) 1759–1766.
- [18] H. Tien, T. Chen, B. Armaly, Vortex instability of natural convection flow over horizontal and inclined plates with uniform surface heat flux, *Numerical Heat Transfer.* 9 (6) (1986) 697–713.
- [19] C. Chen, A. Labhabi, H. Chang, R. Kelly, Spanwise pairing of finite-amplitude longitudinal vortex rolls in inclined free-convection boundary layers, *J. Fluid Mech.* 231 (1991) 73–111.
- [20] A. Tumin, The spatial stability of natural convection flow on inclined plates, *J. Fluids Eng.* 125 (3) (2003) 428–437.
- [21] S. Saha, J. Patterson, C. Lei, Scaling of natural convection of an inclined flat plate: sudden cooling condition, *J. Heat Transfer* 133 (2011) 041503.

- [22] H.-S. Dou, G. Jiang, C. Lei, Numerical simulation and stability study of natural convection in an inclined rectangular cavity, *Math. Probl. Eng.* 2013 (2013) 1–12.
- [23] J. Clarke, N. Riley, Natural convection induced in a gas by the presence of a hot porous horizontal surface, *J. Mechanics and Applied Mathematics.* 28 (4) (1975) 373–396.
- [24] J. Ackroyd, Laminar natural convection boundary layers on near-horizontal plates, *Proc. R. Soc. Lond.* 352 (1669) (1976) 249–274.
- [25] M. Gollner, A. Sánchez, F. Williams, On the heat transferred to the air surrounding a semi-infinite inclined hot plate, *J. Fluid Mech.* 732 (2013) 304–315.
- [26] P. J. Schmid, D. S. Henningson, *Stability and transition in shear flows*, Vol. 142, Springer Science & Business Media, 2012.
- [27] S. Haaland, E. Sparrow, Stability of buoyant boundary layers and plumes, taking account of nonparallelism of the basic flows, *Journal of Heat Transfer* 95 (3) (1973) 295–301.
- [28] P. Hall, The linear development of görtler vortices in growing boundary layers, *J. Fluid Mech.* 130 (1983) 41–58.
- [29] A. Bottaro, P. Luchini, Görtler vortices: Are they amenable to local eigenvalue analysis?, *Eur. J. Mech. B/Fluids* 18 (1) (1999) 47–65.